

NASA Technical Memorandum 58269 NASA-TM-58269 19860000551

Numerical Procedure for Three-Dimensional Hypersonic Viscous Flow Over Aerobrake Configuration

FOR REFERENCE

DO NOT REMOVE FROM THIS BOOK

Chien-peng Li

August 1985

LANGLEY RESEARCH CENTER

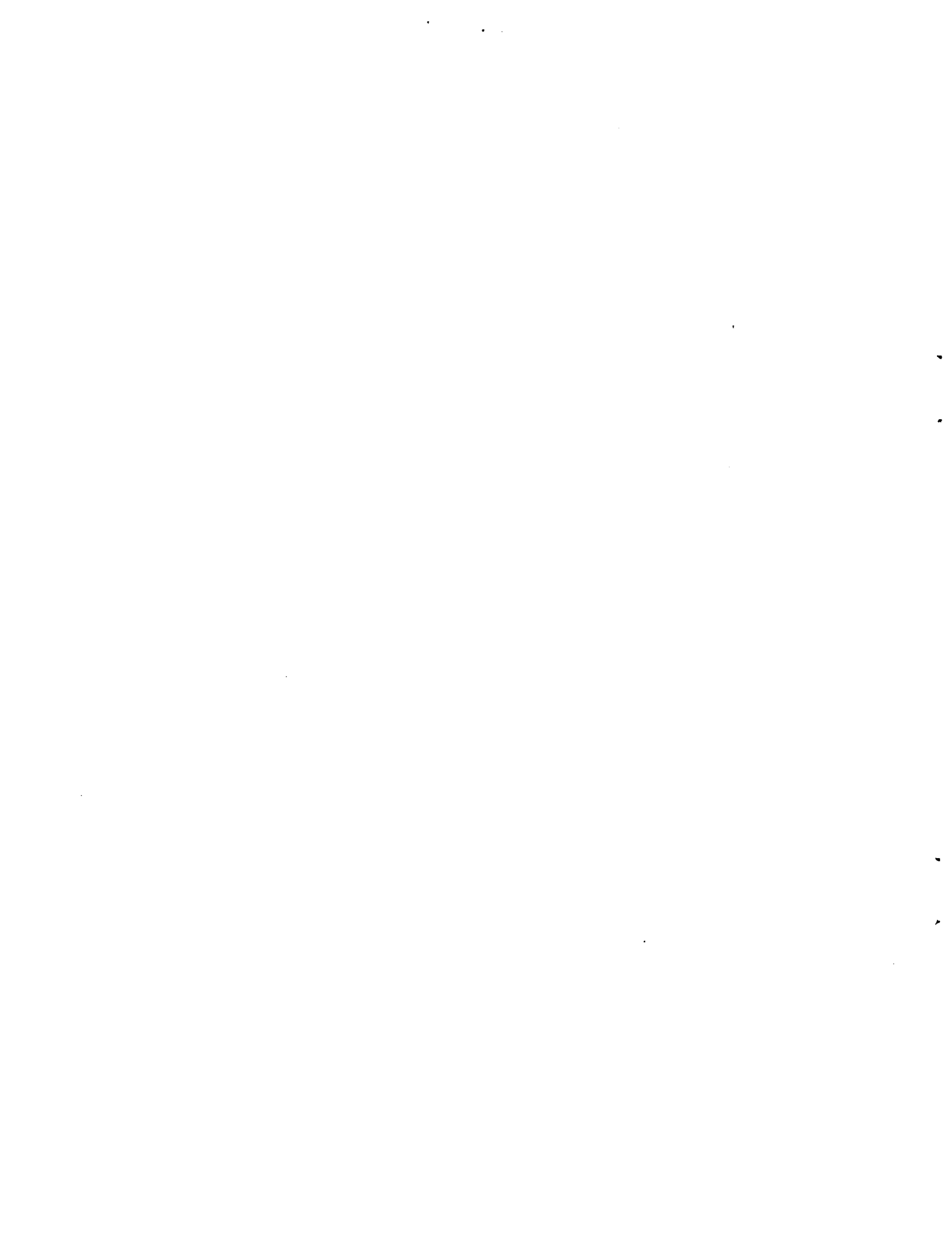
OCT 16 1985

LANGLEY RESEARCH CENTER
LIBRARY, NASA
HAMPTON, VIRGINIA

NASA

National Aeronautics and
Space Administration

Lyndon B. Johnson Space Center
Houston, Texas



NASA Technical Memorandum 58269

**Numerical Procedure for Three-Dimensional Hypersonic
Viscous Flow Over Aerobrake Configuration**

**Chien-peng Li
Lyndon B. Johnson Space Center
Houston, Texas**

N A S A

**National Aeronautics and
Space Administration**

**Scientific and Technical
Information Branch**

1985



CONTENTS

Section		Page
	<u>Abstract</u>	1
1	<u>Introduction</u>	1
2	<u>Coordinate Transformation</u>	2
3	<u>Navier-Stokes Equations in Computational Coordinates</u>	4
4	<u>Treatment of Boundaries</u>	5
5	<u>Initial Conditions</u>	6
6	<u>Numerical Algorithm</u>	6
7	<u>Discussion of Results</u>	8
8	<u>Conclusion</u>	9
	<u>References</u>	9
	<u>Acknowledgment</u>	10

N86-10018 #

FIGURES

Figure		Page
1	Flowfield schematics and physical coordinates	10
2	Sequence of coordinate transformation	
	a) Physical space, X, Y, Z	10
	b) Mapped space, $\bar{X}, \bar{Y}, \bar{Z}$	10
	c) Shear and cluster transformation, $\bar{x}, \bar{y}, \bar{z}$	10
	d) Computational space, x, y, z	10
3	Schematic of computational boundaries	11
4	A perspective view of the flow and Mach contours in $\phi = 0$ and $\pi/2$ planes. (A complete body is shown in the half space.)	11
5	Comparison of shock locations between computation ($\alpha = 18^\circ$) and experiment ($\alpha = 15^\circ$)	11
6	Particle path traces on the pitch plane	11
7	Particle path traces originated from the plane next to the lower pitch plane	11
8	A closeup view of the grid in the base flow region	11
9	Mach contours in the base flow region. (Dashed line = sonic line.)	12
10	Velocity plots in the base flow region	12
11	Pressure contours in the upper pitch plane (normalized by p_∞)	12
12	Temperature contours in the upper pitch plane (normalized by T_∞)	12
13	Pressure distributions on the wall - NS solution	12
14	Pressure distributions on the wall - Euler solution	12

Abstract

A numerical method, which is simpler and more efficient than others currently in use, is proposed for the computation of the full viscous flow over an aerobrake body in hypersonic stream at high altitude. It treats the shock layer surrounding the blunt forebody and the near wake behind the base simultaneously by formulating the Navier-Stokes equations in conformal and azimuthal-angle coordinates. The computational domain is confined by the body wall, outflow surface and the bow shock, which is adjusted along the coordinate normal to the wall in the course of iterations. Because of the optimal grid and a well-developed alternating direction implicit factorization technique for the governing equations, reasonably accurate results can be obtained with a $28 \times 36 \times 7$ grid and 400 time-marching iterations. Excellent agreement of shock location is found between the present result and the schlieren photograph. Details of the base flow and shear-layer impingement on the cylindrical aft body are presented for an adiabatic-wall case.

1. Introduction

Recently, urgent reasons have arisen for finding the complete flowfield solution about a finite-size blunt body flying hypersonically at high altitude. Since ground facilities cannot adequately simulate the flowfield and enable determining the aerodynamic and heating loads needed for designing a spacebound vehicle traveling between low Earth and geosynchronous Earth orbits, analyses will depend on the numerical solution of the model equations. Although computational capability is available to treat three-dimensional (3D) flow over aerodynamic configurations at transonic speeds, straightforward applications of the available methodology to hypersonic flow would require prohibitive amounts of computer time and storage. The favorable approach is to create a grid such that the bow shock and the body become coordinate lines, and the gradients along the body can be properly resolved. Along these directions, a simpler and faster method is proposed to facilitate the grid adaption to the wall and to accelerate the convergence rate of the numerical algorithm. With this method, a reasonably accurate viscous flow solution can be obtained from the full Navier-Stokes (NS) equations on a coarse grid after a few hundred iterations. Of more importance, its performance is equally impressive for flow at high angles of incidence and for arbitrary body shape.

In the hypersonic regime of interest, the turbulence model and geometry details may be considered relatively unimportant compared to the dissociative nature of the air due to high temperature, yet numerical calculations of a finite-body flow are still limited in scope by the computer time and memory and by the numerical algorithms for equations and grid. Nearly all computations have been based on the assumption of laminar flow without finite-rate chemical reactions, and most are for two-dimensional (2D) flows. Lombard et al.(1,2) used a Navier-Stokes formulation on generalized coordinates and simple algebraic grid-clustering equation to study the flowfield of the Galileo probe and of an aerobraking orbital transfer vehicle. The equations are cast in curvilinear coordinates, but the vector variables are defined in Cartesian coordinates. In Ref. 1, an alternating direction implicit (ADI) factorization technique was used, whereas a Gauss-Seidel type relaxation technique was used in Ref. 2 with nearly an order of magnitude reduction in the number of iterations. Gnoffo(3) has introduced an adaptive-grid algorithm to attack similar problems, but used a finite volume and the MacCormack explicit scheme. The grid distribution as determined by weight parameters had enhanced the solution accuracy without adding more grid points to the computational domain. The techniques used in both Ref. 2 and Ref. 3 have undergone continual modifications to improve the accuracy and to reduce the computation time but are restricted to axisymmetric flow currently.

An alternate method was proposed by the author to solve the 3D equations in curvilinear-orthogonal coordinates by a proven ADI factorization technique.(4) The full NS equations are cast in the conformal coordinates defining the planes at constant azimuthal angle. The transformation of a family of ellipsoid-cones resembling the Apollo command module and the Viking aeroshell probe onto a near half-circle is made possible through one application of the Karman-Trefftz equation as suggested by Moretti.(5) Thus, the difficult problem of initializing the complete flow over an arbitrary body becomes a much simpler problem for a sphere. Furthermore, the analytical mapping of coordinates ensures a smaller size of discretization error in a largely deformed grid in comparison to the grid generated by differential equations. The pros and cons of the classical mapping

versus other grid-generation techniques as well as the idea of combining two-dimensional orthogonal grids on slices through the three-dimensional field have been discussed by Ives.⁽⁶⁾

In the present paper, a typical aerobrake configuration consisting of an ellipsoid, a flat disk, and a cylinder is used to demonstrate the capability of the new method. Details of the various coordinate transformations and mappings are described in Sec. 2 of this paper. A derivation of the full NS equations in computational coordinates appears in Sec. 3, followed by a description of computational boundaries in Sec. 4, the definition of initial conditions in Sec. 5, and a discussion of the numerical algorithm in Sec. 6. Results are presented for the aerobrake at an angle of attack of 18°.

2. Coordinate Transformation

The objective is to map the physical domain enclosed by the bow shock, the body, and the plane $Z = \text{constant}$ onto a parallelepiped such that the boundaries become part of the computational coordinates (Fig. 1). The basic fluid-dynamics equations given in orthogonal curvilinear coordinates are used because of their versatility and simplicity to handle the dominant features of the hypersonic flow and a wide variety of body configurations. The equations are expressed in terms of the orthogonal coordinates ξ, η, ζ and their scale factors h_1, h_2, h_3 in the direction of increasing ξ, η, ζ , parallel to unit vectors $\hat{i}, \hat{j}, \hat{k}$. The change in the position vector \vec{r} can then be written as

$$\delta \vec{r} = \hat{i} h_1 d\xi + \hat{j} h_2 d\eta + \hat{k} h_3 d\zeta \quad (1)$$

in which both $(\hat{i}, \hat{j}, \hat{k})$ and (h_1, h_2, h_3) are functions of (ξ, η, ζ) . The physical space used in this study is defined by the spherical coordinates r, θ, ϕ shown in Fig. 1. They are related to Cartesian coordinates X, Y, Z by

$$X = \eta \sin \xi \cos \zeta, Y = \eta \sin \xi \sin \zeta, Z = -\eta \cos \zeta \quad (2)$$

where $\xi = \pi - \theta$, $\eta = r$, and $\zeta = \phi$.

Then, conformal mappings are introduced to transform a given geometry in the $Y = 0$ plane to a near circle in the $Y = 0$ plane. An axisymmetric body can be easily obtained by rotating the circle image around the Z -axis such that each $\zeta = \text{constant}$ plane has the identical image. The mapping is represented by

$$\bar{\xi} = \bar{\xi}(\xi, \eta), \bar{\eta} = \bar{\eta}(\xi, \eta), \bar{\zeta} = \zeta \quad (3)$$

The inverse of Eq. (3) is applied to find the physical image from a given shape in the mapped space. The first use of conformal mapping for numerically analyzing axisymmetric flow over a blunt body was by Van Dyke⁽⁷⁾ in his well-known inverse method, by which both shock and body are conformed to coordinate lines with a single analytical function.

In a direct manner to solve for the flowfield, the body shape is given in physical space, then transformed onto a smooth contour image. A general mapping function, known as the Karman-Trefftz equation, is applied repetitively to remove the corners and edges of complicated geometry.⁽⁵⁾ It is exemplified by

$$\frac{x - h}{x + h^*} = \left(\frac{\bar{x} - 1}{\bar{x} + 1} \right)^{1/\delta} \quad (4)$$

where h and δ are parameters, x and \bar{x} refer to the complex function $x = \xi + i\eta$ and $\bar{x} = \bar{\xi} + i\bar{\eta}$. The conjugate function of h is h^* . The Joukowski equation is a simplification of Eq. (4) by choosing $\delta = 0.5$ and $h = h^* = R(h)$.

The Cauchy-Riemann conditions stated in polar coordinates are

$$\bar{\xi}_\xi = \eta \bar{\eta}_\eta / \bar{\eta} = R(g\chi/\bar{\chi}), \quad \eta \bar{\xi}_\eta = -\bar{\eta}_\xi / \bar{\eta} = I(g\chi/\bar{\chi})$$

where R and I are the real and the imaginary part of the functional $g\bar{x}$, which is composed of

$$g = \frac{d\bar{x}}{d\bar{\chi}} = Ge^{i\omega}, \quad \bar{x} = \bar{\eta}e^{i\bar{\xi}}, \quad \bar{\chi} = \eta e^{i\xi}$$

Note the conformal property implies that $\xi - \bar{\xi} + \omega = 0$; hence, $R(g\bar{x}) = G$ and $I(g\bar{x}) = 0$. The following relations will be used frequently.

$$\bar{\xi}_{\bar{\xi}} = G\eta/\bar{\eta}, \quad \bar{\eta}_{\bar{\eta}} = G, \quad \bar{\xi}_{\eta} = 0, \quad \bar{\eta}_{\xi} = 0 \quad (5)$$

The coefficient of magnification G and the angle of rotation ω vary from point to point.

The change in the position vector \vec{r} now becomes

$$\delta\vec{r} = \hat{i}\bar{h}_1 d\bar{\xi} + \hat{j}\bar{h}_2 d\bar{\eta} + \hat{k}\bar{h}_3 d\bar{\zeta} \quad (6)$$

The scalar factors in the mapped space are $\bar{h}_1 = \bar{\eta}/G$, $\bar{h}_2 = 1/G$, and $\bar{h}_3 = h_3 = \eta \sin \xi$. The next step is to make use of the shear transformation to bring both the outer and the inner boundaries of the domain of interest depicted in the mapped space into becoming a part of the coordinate lines in \bar{x}, \bar{y} . This transformation, shown in Fig. 2c, is accomplished by

$$\bar{x} = \bar{\xi}/\pi, \quad \bar{y} = (\bar{S} - \bar{\eta})/(\bar{S} - \bar{B}), \quad \bar{z} = \bar{\zeta}/2\pi \quad (7)$$

where $\bar{B} = B(\bar{\xi}, \bar{\zeta})$, $\bar{S} = S(\bar{\xi}, \bar{\zeta}, t)$ are the body and shock locations in the mapped space. More algebraic transformation may be used to cluster points toward $\eta = \bar{B}$ or $\xi = \bar{\xi}_c$ and to result in a nonuniform grid in Fig. 2c, but uniformly spaced grid in the computational space, Fig. 2d. The transformation equations used are as follows:

$$\begin{aligned} x &= \left[c + \operatorname{arcsinh} \left(\frac{\bar{x}}{\bar{x}_c} - 1 \right) \sinh(\omega c)/\omega \right] / \bar{x} \\ c &= \ln \left[\left[1 + (\exp(\omega) - 1) \frac{\bar{x}}{\bar{x}_c} \right] / \left[1 + (\exp(-\omega) - 1) \frac{\bar{x}}{\bar{x}_c} \right] \right] / 2\omega \\ y &= \ln \left[\left(\beta + \bar{y} \right) / \left(\beta - \bar{y} \right) \right] / \ln \left[\left(\beta + 1 \right) / \left(\beta - 1 \right) \right] \\ z &= \bar{z} \end{aligned} \quad (8)$$

where β and ω are used to control the degree of clustering.

The transformations between the computational and the physical space are summarized schematically in Fig. 2. The mapped coordinates are given by Eq. (4); the velocity components at each point are decomposed on a local polar frame which is rotated by $\omega = \xi - \bar{\xi}$. The computational coordinates are determined by Eqs. (7) and (8); velocity components are identical to those in the mapped space.

3. Navier-Stokes Equations in Computational Coordinates

The conservative law of a single-component, compressible, viscous flow is commonly written in terms of orthogonal curvilinear coordinates ξ, η, ζ or $\bar{\xi}, \bar{\eta}, \bar{\zeta}$. To recast the governing equations in terms of computational coordinates, repetitive applications of chain rule are needed to result in the following form.

$$u_t + f_x + g_y + h_z + r = 0 \quad (9)$$

where $u = \bar{h}_1 \bar{h}_2 \bar{h}_3 \bar{u}$, $f = \bar{h}_2 \bar{h}_3 \bar{x}_\xi \bar{f}$, $g = \bar{h}_1 \bar{h}_3 \bar{y}_\eta \bar{g} + \bar{h}_3 \bar{h}_1 \bar{y}_\eta \bar{g} + \bar{h}_1 \bar{h}_2 \bar{y}_\zeta \bar{h} + \bar{h}_1 \bar{h}_2 \bar{h}_3 \bar{y}_t \bar{u}$,

$$h = \bar{h}_1 \bar{h}_2 \bar{z}_\zeta \bar{h},$$

$$r = \begin{bmatrix} 0 \\ h_3 (\bar{h}_1)_\eta \bar{f}(3) - h_3 (\bar{h}_2)_\xi \bar{g}(3) - \bar{h}_2 (h_3)_\xi \bar{h}(4) \\ h_3 (\bar{h}_2)_\xi \bar{f}(3) - \bar{h}_1 (h_3)_\eta \bar{h}(4) - h_3 (\bar{h}_1)_\eta \bar{f}(2) \\ \bar{h}_2 (h_3)_\xi \bar{h}(2) + \bar{h}_1 (h_3)_\eta \bar{h}(3) \\ 0 \end{bmatrix}$$

$$\bar{u} = \begin{bmatrix} \rho \\ \rho \bar{u} \\ \rho \bar{v} \\ \rho w \\ \rho \varepsilon \end{bmatrix}, \quad \bar{f} = \begin{bmatrix} \rho \bar{u} \\ \rho \bar{u}^2 + \pi_{\xi\xi}^- \\ \rho \bar{u}\bar{v} + \pi_{\xi\eta}^- \\ \rho \bar{u}w + \pi_{\xi\zeta}^- \\ \rho \bar{u}\varepsilon + \phi_\xi^- \end{bmatrix}, \quad \bar{g} = \begin{bmatrix} \rho \bar{v} \\ \rho \bar{v}\bar{u} + \pi_{\eta\xi}^- \\ \rho \bar{v}^2 + \pi_{\eta\eta}^- \\ \rho \bar{v}w + \pi_{\eta\zeta}^- \\ \rho \bar{v}\varepsilon + \phi_\eta^- \end{bmatrix}, \quad \bar{h} = \begin{bmatrix} \rho w \\ \rho w \bar{u} + \pi_{\zeta\xi}^- \\ \rho w \bar{v} + \pi_{\zeta\eta}^- \\ \rho w^2 + \pi_{\zeta\zeta}^- \\ \rho w \varepsilon + \phi_\zeta^- \end{bmatrix}$$

The scalar factors are defined in Eq. (6), and the metric coefficients of the nonorthogonal coordinate transforms are analytic. Convective and diffusive fluxes in the NS equations have standard notation. The velocity components \bar{u}, \bar{v} are equal to

$$\begin{pmatrix} \bar{u} \\ \bar{v} \end{pmatrix} = \begin{pmatrix} \cos \omega & -\sin \omega \\ \sin \omega & \cos \omega \end{pmatrix} \begin{pmatrix} u \\ v \end{pmatrix}, \text{ where } \omega = \bar{\xi} - \xi$$

Other variables as well as the stress tensor and heat-flux vector can be found from standard texts.

A set of simplified equations deduced from Eq. (9) by eliminating h_3 is used on $x = 0$ and π , as follows.

$$u_t + f_x + g_y + r = 0 \quad (10)$$

where $u = \bar{h}_1 \bar{h}_2 \bar{u}$, $f = (2 - u^*/u) \bar{h}_2 \bar{x}_\xi \bar{f} + \bar{h}_z - uu^*$, $g = \bar{h}_2 \bar{y}_\eta \bar{g} + \bar{h}_1 \bar{y}_\eta \bar{g} + \bar{h}_1 \bar{h}_2 \bar{y}_t \bar{u}$

$$r = \begin{bmatrix} \bar{g}(1) \\ \bar{g}(2) + (\bar{h}_1)_{\bar{\eta}} \bar{f}(3) - (\bar{h}_2)_{\bar{\xi}} - \bar{g}(3) \\ \bar{g}(3) + (\bar{h}_2)_{\bar{\xi}} \bar{f}(3) - \bar{h}_1 \bar{h}_2 \bar{h}(4)/h_3 - (\bar{h}_1)_{\bar{\eta}} \bar{f}(2) \\ 0 \\ \bar{g}(5) \end{bmatrix}$$

The derivatives of $(h_3)_{\bar{\xi}}$ and $(h_3)_{\bar{\eta}}$ are obtained by making use of the chain rule; hence,

$$(h_3)_{\bar{\xi}} = \xi_{\bar{\xi}} (h_3)_{\xi} = \bar{h}_1 \cos \xi \text{ and } (h_3)_{\bar{\eta}} = \eta_{\bar{\eta}} (h_3)_{\eta} = \bar{h}_2 \sin \xi$$

Other derivatives of \bar{h}_1 and \bar{h}_2 , however, must be numerically determined using the following equations.

$$\left(\frac{\quad}{\xi}\right)_{\bar{\xi}} = x_{\bar{\xi}} \left(\frac{\quad}{\xi}\right)_x + y_{\bar{\xi}} \left(\frac{\quad}{\xi}\right)_y, \quad \left(\frac{\quad}{\eta}\right)_{\bar{\eta}} = y_{\bar{\eta}} \left(\frac{\quad}{\eta}\right)_y$$

4. Treatment of Boundaries

The outer boundary consists of three segments, denoted by 1, 2, and 3 in Fig. 3. Segment 1, ranging from $0 \leq \xi \leq \xi_{max}$, is the bow shock, which varies in position according to the equation

$$\hat{n} \bar{S}^{k+1} = \hat{n} \bar{S}^k + n (\bar{S}_t)^k \Delta t \quad (11)$$

where \bar{S}_t^k is estimated at the end of each iteration k by matching the Rankine-Hugoniot (RH) results to the flowfield results. When the computation converges, the shock position will not change since $\bar{S}_t = 0$. Segment 2 represents a cone with a half-angle determined by the shock slope at $\xi = \xi_{max}$. The cone terminates at the plane $Z = Z_w$, a specified parameter to control the extent of computation region. The radial location of segments 2 and 3 is given by simple equations. The conic shock wave has no speed, so the RH equations alone are used to define the flow variables. The outflow surface, segment 3, has inviscid outward supersonic flow for its major portion; two-point extrapolation formula is considered adequate for prescribing flow variables therein.

Let S^* be the shock location along η at $\bar{\xi}^* = \pi - \theta_{max}$; the cone is governed by the following equation.

$$\bar{S} = \bar{S}^* \left(\sin \bar{\theta}^* - \cos \bar{\theta}^* \tan \left(\bar{\theta} + \bar{\theta}^* - \pi/2 \right) \right) / \left(\sin \bar{\theta} - \cos \bar{\theta} \tan \left(\bar{\theta} + \bar{\theta}^* - \pi/2 \right) \right)$$

The outflow surface is given by

$$\bar{S} = Z_w \sec \bar{\theta}', \text{ where } \bar{\theta}' = \arctan \left(\left(\bar{S}^* + Z_w \tan \bar{\theta}^* \right) / Z_w \right)$$

The corner of segments 2 and 3 is given by

$$\bar{\theta}_{cr} = \arctan \left[\left(\bar{S}^* \sin \bar{\theta}^* - \left(Z_w - \bar{S}^* \cos \bar{\theta}^* \right) \tan \left(\bar{\theta} + \bar{\theta}^* - \pi/2 \right) \right) / Z_w \right]$$

The velocity vector on the boundary first is computed in (ξ, η, ζ) components from Eq. (9), then is adjusted to satisfy the RH equations at the bow and conic shocks, and to meet the vanishing normal or no-slip conditions at the wall. In either case, an intrinsic coordinate system is needed to relate the local normal, tangent, and binormal vectors $(\hat{n}, \hat{t}, \hat{b})$ to the physical orientation vectors (i, j, k) . Let the body and the outer surface be $b = \eta - B(\xi, \zeta)$ and $s = \eta - S(\xi, \zeta)$, respectively; the corresponding normal vector \hat{n} is $(-B_{\xi}/B, 1, -B_{\zeta}/(B \sin \xi))$ and $(S_{\xi}/S, -1,$

$S_\zeta/(S \sin \xi)$), which are meant to point inward the computational domain. Other components of the intrinsic frame are obtained from $\hat{t} = \hat{n} \times \hat{K}$, and $\hat{b} = \hat{t} \times \hat{n}$. The procedures of shock fitting and wall velocity adjustment are identical to those described in Ref. 4, with the exception that u, v are obtained from \bar{u}, \bar{v} from

$$\begin{pmatrix} u \\ v \end{pmatrix} = \begin{pmatrix} \cos \omega & \sin \omega \\ -\sin \omega & \cos \omega \end{pmatrix} \begin{pmatrix} \bar{u} \\ \bar{v} \end{pmatrix}, \text{ where } \omega = \bar{\xi} - \xi$$

After the boundary conditions have been imposed, an inverse transformation is used to get \bar{u}, \bar{v} .

Velocity conditions may be imposed on the boundaries using the mapped coordinates. The unit normals to the shocks and the body are, respectively, equal to $(-\bar{B}_\zeta/\bar{h}_1, 1/\bar{h}_2, -\bar{B}_\zeta/\bar{h}_3)$, $(\bar{S}_\zeta/\bar{h}_1, -1/\bar{h}_2, \bar{S}_\zeta/\bar{h}_3)$. The zero body normal velocity is automatically satisfied in the physical space. Upstream, at the shock surface, the free-stream velocity components are cast in terms of the mapped coordinates by inverse transformation.

5. Initial Conditions

Two sets of flow variables are specified along the outer and inner boundaries. An initial estimate of shock has two parts.

$$\bar{S} = \bar{B} + \bar{\delta} (1 + (\bar{\xi})^e) \text{ for } \bar{\xi} \leq \bar{\xi}_{cl} \text{ and } \bar{S} = \bar{B} + \bar{\delta} (1 + d\bar{\xi}) \text{ for } \bar{\xi} > \bar{\xi}_{cl}$$

where d and e are input parameters for specifying shock shape; $\bar{\delta}$ is the standoff distance. Using the RH equations, shock properties are obtained consistent with the slope. On the body, the Newtonian pressure and the isentropic equation are used to prescribe variables for $\bar{\xi} \leq \bar{\xi}_{cl}$, and base flow approximations wall density $\rho_w = 0.25\rho_\infty$; energy $e = C_v T_\infty$, where C_v is specific heat at constant volume and T is temperature; velocity components $u = v = w = 0$ are applied to the rest of the body, $\bar{\xi} > \bar{\xi}_{cl}$; $\bar{\xi}_{cl}$ is the body point where the body normal first turns into the free-stream vector starting from the stagnation point. The outflow surface has properties varying from the shock values at the juncture point between segments 2 and 3 to the free-stream condition at $\bar{\xi} = \pi$. Once the two lines are known, a simple interpolation is used to estimate the initial values in the computational space. The same procedure is valid if physical coordinates are used in the computation.

6. Numerical Algorithm

The computation space (x, y, z) is discretized into a three-dimensional network of grid points, which are defined by

$$x_m = (m-2)\Delta x, y_n = (n-2)\Delta y, z_\ell = (\ell-2)\Delta z$$

with $\Delta x = 1/(mc-2)$, $\Delta y = 1/(nc-2)$, $\Delta z = 1/(lc-2)$, and $m = 1, 2, \dots, mc$, $n = 2, 3, \dots, nc$, and $\ell = 1, \dots, lcp$, where $lcp = lc + 1$. The subscripts m and ℓ cover a range of grid points beyond the computation domain in order to incorporate the boundary conditions. The relations indicate that any point in the computation space can be addressed by the intersection of three independent families of coordinate lines, but the metrics and the dependent variables still require three-dimensional arrays such as $\rho_{n,m,\ell} = \rho(x_m, y_n, z_\ell)$.

The resultant finite-difference counterpart of Eq. (9) is

$$\delta_t^+ u + \delta_x f + \delta_y g + \delta_z h + r_{n,m,\ell} = 0 \tag{12}$$

where δ_t^+ denotes the two-point operator, and δ_x, δ_y , and δ_z are centered spatial operators except along $n = nc$ at time level $k + 1$.

The spatial approximations are solved simultaneously with the unknown vector $u_{n,m,\ell}^{k+1}$ to allow greater changes of $\delta_t^+ u$ and, hence, to result in a faster rate of convergence from initial approximations to the final solution. A factorization technique due to Beam and Warming⁽⁸⁾ which emphasizes the noniterative nature of the well-established ADI method and solves for the incremental vector of the conservative variable u has been adopted and modified. In this version, because the primitive variables $v = (\rho, u, v, w, e)^T$ are used, the Jacobian matrices have simpler expression and involve less arithmetic. The solution procedure comprises five steps.

$$\begin{aligned}
\tau \Delta u_{n,m,\ell}^k &= -\delta_x f^k - \delta_y g^k - \delta_z h^k - r_{n,m,\ell}^k \\
\left(\tau I + \delta_x A - \delta_{xx} (D + \tau d_I I) \right) \Delta v_{n,m,\ell}^* &= \tau P^{-1} \left(\Delta u_{n,m,\ell}^k - d_e \delta^4 u_{n,m,\ell}^k \right) \\
\left(\tau I + \delta_y B - \delta_{yy} (E + \tau d_I I) \right) \Delta v_{n,m,\ell}^{**} &= \tau \Delta v_{n,m,\ell}^* \\
\left(\tau I + \delta_z C - \delta_{zz} (F + \tau d_I I) \right) \Delta v_{n,m,\ell}^{k+1} &= \tau \Delta v_{n,m,\ell}^{**} \\
v_{n,m,\ell}^{k+1} &= v_{n,m,\ell}^k + \Delta v_{n,m,\ell}^{k+1}
\end{aligned} \tag{13}$$

where τ is the inverse of the local Δt multiplied by a constant Courant number, and d_I and d_e are the implicit and explicit damping coefficients. Each of the three equations in the middle of Eq. (13) represents a tridiagonal system of linear equations with 5 by 5 matrix coefficients.

It is seen in Eq. (13) that the first step is to find the residual explicitly, then to smooth or to filter out the localized errors in $\Delta u_{n,m,\ell}^k$ by subsequent implicit steps performed along each coordinate. Obviously, the implicit calculations are not needed for numerical stability consideration alone if $\Delta t_{n,m,\ell}$ meet the Courant-Friedrich-Lewy (CFL) criterion, or any step can be deleted if $(\Delta t_i)_{min} > CN(\Delta t_{n,m,\ell})_{min}$, where $i = n, m$, or ℓ and CN denotes the Courant number. Nevertheless, the primary function of implicit solutions seems to be more in the acceleration of the overall rate of convergence than in maintaining solution stability. Numerical experiments have suggested that implicit solution is even preferable (without concern in computation cost) to the explicit solution because the effect of boundaries can be transmitted across the entire line.

The Jacobian matrices of the convective and diffusive fluxes with respect to v are given as follows.

$$\begin{aligned}
\Delta \bar{u} &= \bar{P} \Delta \bar{v} \\
\Delta \bar{f} &= \bar{P}\bar{A} \Delta \bar{v} + \bar{P}\bar{D} \Delta \bar{v}_x \\
\Delta \bar{g} &= \bar{P}\bar{B} \Delta \bar{v} + \bar{P}\bar{E} \Delta \bar{v}_y \\
\Delta \bar{h} &= \bar{P}\bar{C} \Delta \bar{v} + \bar{P}\bar{F} \Delta \bar{v}_z
\end{aligned} \quad \text{where } \bar{P} = \bar{h}_1 \bar{h}_2 \bar{h}_3 \quad \text{and } q = (\bar{u}^2 + \bar{v}^2 + \bar{w}^2)/2$$

$$\begin{bmatrix}
1 & 0 & 0 & 0 & 0 \\
\bar{u} & \rho & 0 & 0 & 0 \\
\bar{v} & 0 & \rho & 0 & 0 \\
w & 0 & 0 & \rho & 0 \\
q & \rho \bar{u} & \rho \bar{v} & \rho w & \rho
\end{bmatrix}$$

The components of the Jacobian matrices are as follows.

$$\begin{aligned}
A_{11} &= u x_{\xi} / \bar{h}_1 + w x_{\zeta} / h_3, \quad A_{12} = \rho x_{\xi} / \bar{h}_1, \quad A_{13} = \rho x_{\zeta} / h_3, \quad A_{21} = g e x_{\xi} / (\rho \bar{h}_1), \quad A_{22} = A_{11}, \quad A_{15} = (\gamma - 1) x_{\xi} / \bar{h}_1 \\
A_{33} &= A_{11}, \quad A_{41} = g e x_{\xi} / (\rho \bar{h}_1), \quad A_{44} = A_{11}, \quad A_{45} = (\gamma - 1) x_{\zeta} / h_3, \quad A_{52} = p x_{\xi} / (\rho \bar{h}_1), \quad A_{54} = p x_{\zeta} / (\rho h_3), \quad A_{55} = A_{11} \\
B_{11} &= u y_{\xi} / \bar{h}_1 + v y_{\eta} / \bar{h}_2 + w y_{\zeta} / h_3, \quad B_{12} = \rho y_{\xi} / \bar{h}_1, \quad B_{13} = \rho y_{\eta} / \bar{h}_2, \quad B_{14} = \rho y_{\zeta} / h_3, \quad B_{21} = g e y_{\xi} / (\rho \bar{h}_1) \\
B_{22} &= B_{11}, \quad B_{25} = (\gamma - 1) y_{\xi} / \bar{h}_1, \quad B_{31} = g e y_{\eta} / (\rho \bar{h}_2), \quad B_{33} = B_{11}, \quad B_{35} = (\gamma - 1) y_{\eta} / \bar{h}_2, \quad B_{41} = g e y_{\zeta} / (\rho h_3) \\
B_{44} &= B_{11}, \quad B_{45} = (\gamma - 1) y_{\zeta} / h_3, \quad B_{52} = p y_{\xi} / (\rho \bar{h}_1), \quad B_{53} = p y_{\eta} / (\rho \bar{h}_2), \quad B_{54} = p y_{\zeta} / (\rho h_3), \quad B_{55} = B_{11}
\end{aligned}$$

$$\begin{aligned}
C_{11} &= wz_{\zeta}/h_3, C_{14} = \rho z_{\zeta}/h_3, C_{22} = C_{11}, C_{33} = C_{11} \\
C_{41} &= gez_{\zeta}/(\rho h_3), C_{44} = C_{11}, C_{54} = \rho z_{\zeta}/(\rho h_3), C_{55} = C_{11} \\
D_{22} &= 4\mu x_{\xi}^2/(3\rho \bar{h}_1^2) + \mu x_{\zeta}^2/(\rho h_3^2), D_{33} = \mu x_{\xi}^2/(\rho \bar{h}_1^2) + \mu x_{\zeta}^2/(\rho h_3^2) \\
D_{44} &= \mu x_{\xi}^2/(\rho \bar{h}_1^2) + 4\mu x_{\zeta}^2/(3\rho h_3^2), D_{55} = k(\gamma - 1)(x_{\xi}^2/\bar{h}_1^2 + x_{\zeta}^2/h_3^2)/\rho \\
E_{22} &= 4\mu y_{\xi}^2/(3\rho \bar{h}_1^2) + \mu y_{\eta}^2/(\rho \bar{h}_2^2) + \mu y_{\zeta}^2/(\rho h_3^2), E_{23} = \mu y_{\xi} y_{\eta}/(3\rho \bar{h}_1 \bar{h}_2), E_{24} = \mu y_{\xi} y_{\zeta}/(3\rho \bar{h}_1 h_3) \\
E_{32} &= \mu y_{\eta} y_{\xi}/(3\rho \bar{h}_1 \bar{h}_2), E_{33} = E_{22}, E_{34} = \mu y_{\eta} y_{\zeta}/(3\rho \bar{h}_2 h_3), E_{42} = \mu y_{\zeta} y_{\xi}/(3\rho h_3 \bar{h}_1) \\
E_{43} &= \mu y_{\zeta} y_{\eta}/(3\rho h_3 \bar{h}_2), E_{44} = E_{11}, E_{45} = (\gamma - 1)k(y_{\xi}^2/\bar{h}_1^2 + y_{\eta}^2/\bar{h}_2^2 + y_{\zeta}^2/h_3^2)/\rho \\
F_{22} &= \mu z_{\zeta}/(\rho h_3^2), F_{33} = F_{22}, F_{44} = 4\mu z_{\zeta}/(3\rho h_3^2), F_{55} = (\gamma - 1)k^2 z_{\zeta}/(\rho h_3^2)
\end{aligned}$$

The subscripts refer to the components of the rate-of-strain tensor. If the components are zero, they are not shown.

7. Discussion of Results

The method presented in Secs. 2 through 6 has been implemented into an operational code on a Univac 82 system (equivalent to a Control Data Corporation (CDC) 6600) with a maximum storage of 263k words. The reason for selecting this aerobrake configuration for computational studies is that test data are available from the wind-tunnel and ballistic range, which are useful to check the method. The flow pattern observed in experiments indicates strong expansion over the shoulder, and the separating boundary layer on the back quickly merges into the near wake. A coupled solution of the shock layer in front of the nose and the flow surrounding the cylinder is deemed necessary to accurately predict the turning of the boundary layer and the base flow area.

The code is designed to perform the flow simulation for a realistic spacecraft in the continuum regime between 75 to 90 km and 9 to 12 km/s in altitude and speed, respectively. The major axis of the blunt frontal face has a magnitude between 6 and 10 m. The Reynolds number for this vehicle is in the range of 0.3×10^6 to 0.5×10^6 . The shock layer has a distinguishable viscous layer and a laminar near wake. For the present purpose of developing a computational method, a simple equation of state is used. The body is configured to have an ellipsoid with axis ratio 3:1, which is truncated by a flat disk and attached to a cylinder of radius equal to 1/3 and length equal to the radius of the disk. A smooth contour is obtained in the mapped plane through four successive applications of Eq. (4). The hinge points, h , are located near the corners and edges of the aerobrake, shown in Fig. 2. The resultant mapped contour is closer to a pear shape than to a near circle; hence, the grid lines on top of the cylinder are still somewhat skewed. The origin of the physical polar coordinate system is located between the geometric center of the ellipsoid and the disk, so as to enable definition of the geometry by a single-valued function of θ .

An initial grid of $10 \times 36 \times 7$ ($N \times M \times L$) was first used to solve the Euler equations with as many as 300 iterations. Then, a viscous grid of $28 \times 36 \times 7$ was used to perform 400 more iterations. Despite the fact that an initial estimate for a 3D flowfield is always more difficult than for a 2D flowfield, the procedure given in Sec. 5 is found to be quite satisfactory. At the end of 300 iterations, the Euler solution is generally converged in terms of S_t and p_w . Using the inviscid results to start the iteration for the viscous solution, changes of flow variables are mainly within the viscous layer and the near wake. The criteria of a converged viscous calculation is therefore based on the wall friction and heat-transfer coefficients, C_F and C_H , respectively. It has been noted

that these results tend to vary slightly from their mean values, and an accuracy level beyond the fourth-place digit can not be expected from the grid. More numerical experiments to investigate the effect of C_N , damping parameters, and number of iterations have been reported in Ref. 9. The use of appended damping terms is critical to the success of the ADI computations. The procedures developed for blunt-body flow problems (Ref. 9) are found useful for the present finite-body problems.

The computation time was approximately 6 hr central processing unit (CPU) for 100 iterations. The implicit procedure consumes 50% of the total time to set up the Jacobian matrices and to solve the block tri-diagonal equations. The mapping is estimated to use only 5% of the total time. The free-stream conditions are $M = 34.8$, $Re = 8270$, $\alpha = 18^\circ$, and $R_N = 7$ m.

Figure 4 is a perspective view of the flowfield, wherein the upper portion of the pitch plane and the meridional plane at $\phi = \pi/2$ have the shock wave and Mach contours. A half of the body is shown in the background; some of the grid is removed for clarity. The shock location compares favorably with the schlieren photograph taken from the NASA Langley Research Center hypersonic wind tunnel at $M = 10(10)$ despite the different body geometries (Fig. 5). Another perspective view of the body is shown in Fig. 6, along with the trajectories of particles which move into the pitch planes on top of and behind the cylindrical body. Most of the particles follow the expected direction. The ring vortex and the crossflow downstream of the disk interact strongly and produce very intriguing flow patterns resembling a form of the trailing vortex behind a wingtip (Fig. 7). A closeup view of the grid is exhibited in Fig. 8. The grid is optimally distributed on the frontal face and packed toward the wall. A plot of Mach contours (Fig. 9) is used to study the shear-layer impingement on the lower portion of the cylinder. Sonic lines are plotted in dashed segments. Extensive recirculation areas are seen in Fig. 10 by means of velocity plot. The ring vortex starts at the sharp edge of the blunt nose and ends on the surface of the cylinder. The separation point of the boundary layer is further inward on the windward pitch plane as one would expect. The boundary-layer profile on the blunt face is also of strong interest, since it shares the same characteristics as observed in a low-speed plane stagnation flow. Lack of streamwise velocity gradient prevents development of the boundary layer as conventionally defined. Pressure and temperature contours are shown in Figs. 11 and 12, respectively, on the upper pitch plane. An expansion fan is observed between the body edge and the conic shock wave, and the near wake has a temperature range close to one-half the stagnation temperature.

The viscous pressure distribution is given in Fig. 13. The flow incidence angle has shifted the distribution to the negative x -axis. The base pressure is on the order of 10% the dynamic pressure. The pressure level on the upper disk is higher than that on the lower disk, because the flow speeds are different in those regions. Finally, the inviscid pressure distribution is given in Fig. 14 for comparative purpose. The edge effect is transmitted upstream and affects nearly 70% of the blunt face.

8. Conclusion

A method is proposed to reduce computational labor and storage requirement by taking advantage of the features in conformal mapping and the proven performance of an ADI factorization shock-fitting algorithm. In contrast to the methods based on the generalized coordinates, the number of metrics and the truncation error are minimized, the rate of convergence is substantially accelerated, and the level of accuracy is higher for the same number of grid points. The ADI technique is potentially competitive with the developing relaxation methods in the execution of large three-dimensional hypersonic problems on vector computers. In the continual effort of certifying the present method, more quantitative comparisons with test data are being planned.

References

1. Lombard, C. K., Davy, W. C., and Green, M. J., "Forebody and Base Region Real-Gas Flow in Severe Planetary Entry by a Factored Implicit Numerical Method - Part 1," AIAA Paper 80-0065, 18th Aerospace Sciences Meeting, Pasadena, Calif., Jan. 14-16, 1980.
2. Lombard, C. K., Venkatapathy, E., and Bardina, J., "Forebody and Baseflow of a Dragbrake OTV by an Extremely Fast Single Level Implicit Algorithm," AIAA Paper 84-1699, 17th Fluid Dynamics, Plasma Dynamics, and Laser Conference, Snowmass, Colo., June 25-27, 1984.
3. Gnoffo, P. A., "A Finite-Volume, Adaptive Grid Algorithm Applied to Planetary Entry Flowfields," AIAA Journal, Vol. 21, No. 9, Sept. 1983, pp. 1249-1254.
4. Li, C. P., "Computational Methods for Hypersonic Viscous Flow Over Finite Ellipsoid-Cones at Incidence," AIAA Paper 85-0925, 20th Thermophysics Conference, Williamsburg, Va., June 19-21, 1985.

5. Moretti, G., "Conformal Mappings for Computations of Steady, Three-Dimensional, Supersonic Flows," Numerical/Laboratory Computation Methods in Fluid Mechanics, ed. A. A. Pouring and V. I. Shah, ASME Publications, 13, 1976, pp. 13-28.
6. Ives, D. C., "Quasi Three-Dimensional Grid Generation Using Conformal Mapping," AIAA Paper 83-1906, Computational Fluid Dynamics Conference, Danvers, Mass., July 12-14, 1983.
7. Van Dyke, M. D., "The Supersonic Blunt-Body Problem - Review and Extension," Journal of the Aerospace Sciences, Vol. 25, 1958, pp. 485-496.
8. Beam, R. and Warming, R. F., "An Implicit Factored Scheme for the Compressible Navier-Stokes Equations," AIAA Journal, Vol. 16, Apr. 1978, pp. 393-401.
9. Li, C. P., "A Three-Dimensional Navier-Stokes/Euler Code for Blunt-Body Flow Computations," AIAA Paper 85-0361, 23rd Aerospace Sciences Meeting, Reno, Nev., Jan. 14-17, 1985, or NASA TM-58266, 1985.
10. Blackstoke, T., private communication.

Acknowledgment

The author wishes to thank Ray Gomez of the NASA Lyndon B. Johnson Space Center for making some of the plots and P. Buning of the NASA Ames Research Center for providing his graphic code.

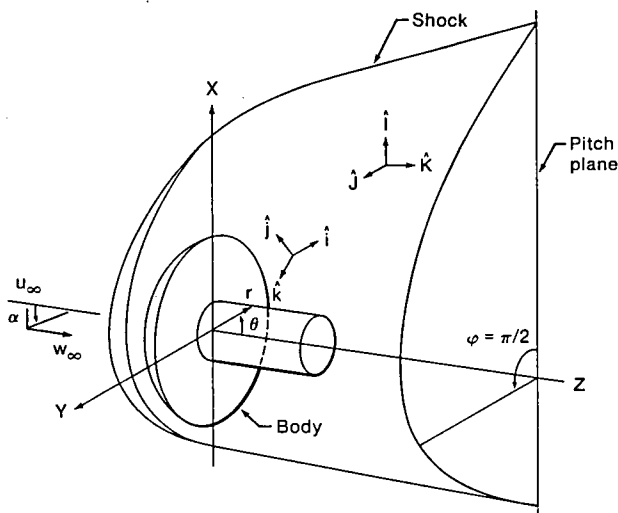


Fig. 1 Flowfield schematics and physical coordinates.

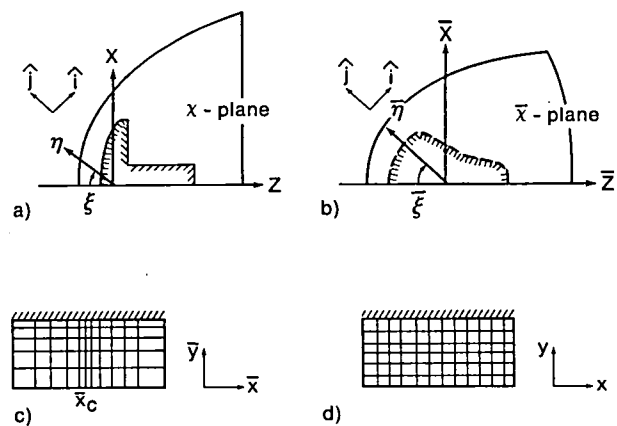


Fig. 2 Sequence of coordinate transformation.
a) Physical space, X, Y, Z . b) Mapped space, $\bar{X}, \bar{Y}, \bar{Z}$. c) Shear and cluster transformation, \bar{x}_c, \bar{y} . d) Computational space, x, y, z .

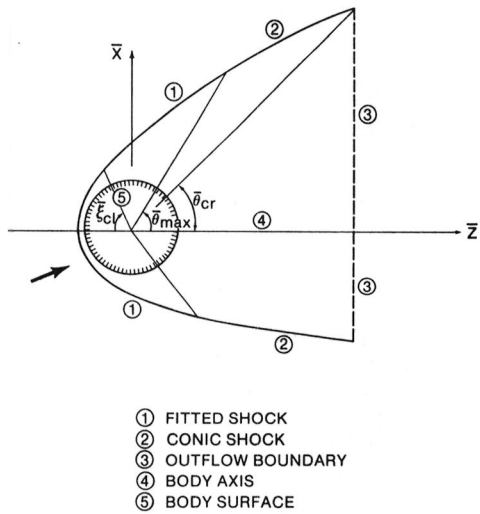


Fig. 3 Schematic of computational boundaries.

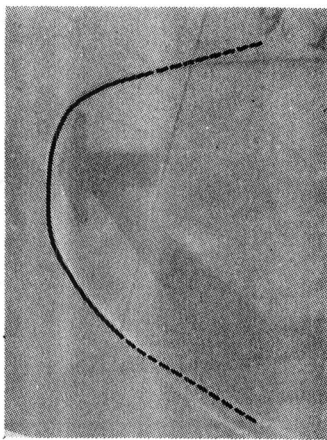


Fig. 5 Comparison of shock locations between computation ($\alpha = 18^\circ$) and experiment ($\alpha = 15^\circ$).

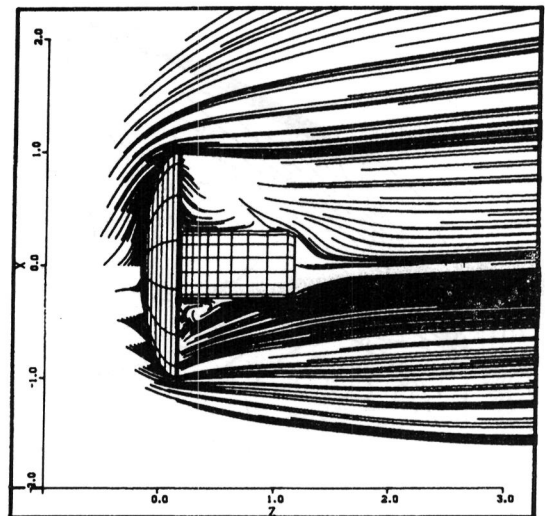


Fig. 6 Particle path traces on the pitch plane.

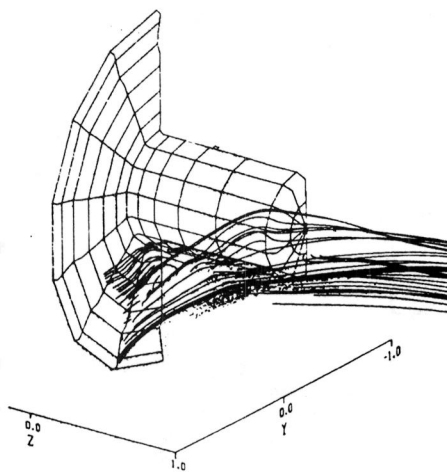


Fig. 7 Particle path traces originated from the plane next to the lower pitch plane.

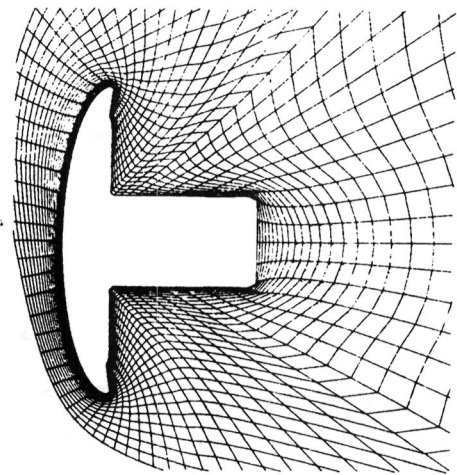


Fig. 8 A closeup view of the grid in the base flow region.

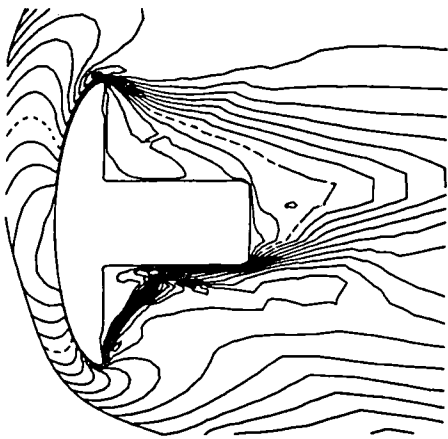


Fig. 9 Mach contours in the base flow region.
(Dashed line = sonic line.)

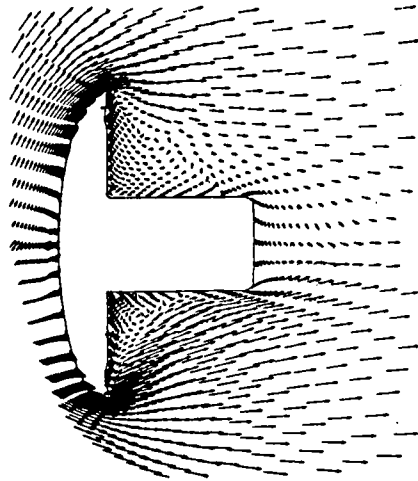


Fig. 10 Velocity plots in the base flow region.

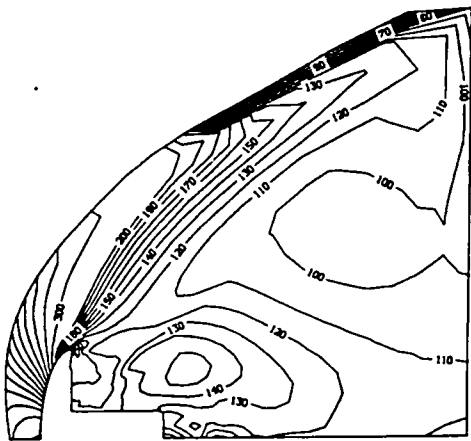


Fig. 11 Pressure contours in the upper pitch plane
(normalized by p_∞).

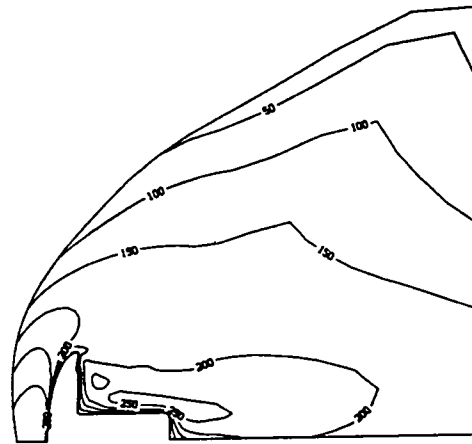


Fig. 12 Temperature contours in the upper pitch plane
(normalized by T_∞).

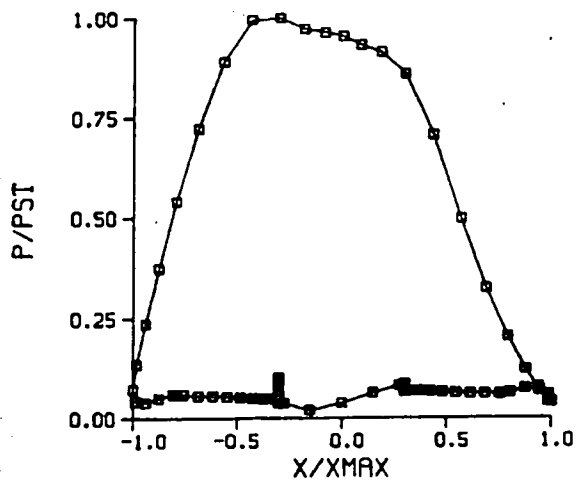


Fig. 13 Pressure distributions on the wall - NS solution.

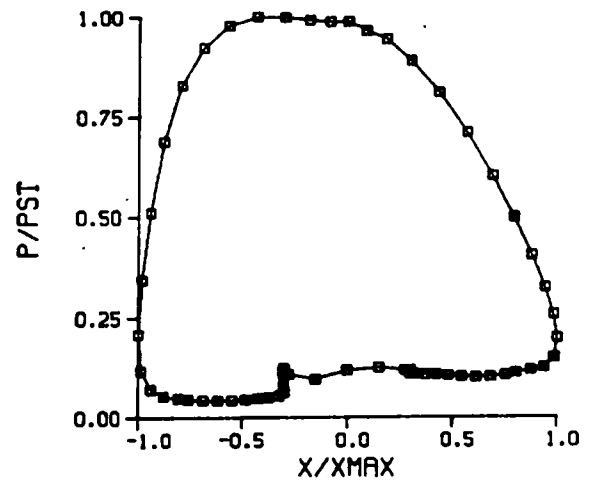


Fig. 14 Pressure distributions on the wall - Euler solution.

1. Report No. NASA TM-58269	2. Government Accession No.	3. Recipient's Catalog No.	
4. Title and Subtitle NUMERICAL PROCEDURE FOR THREE-DIMENSIONAL HYPERSONIC VISCIOUS FLOW OVER AEROBRAKE CONFIGURATION		5. Report Date August 1985	
		6. Performing Organization Code 953-36-00-00-72	
7. Author(s) Chien-peng Li		8. Performing Organization Report No. S-549	
		10. Work Unit No.	
9. Performing Organization Name and Address Lyndon B. Johnson Space Center Houston, Texas 77058		11. Contract or Grant No.	
		13. Type of Report and Period Covered Technical Memorandum	
12. Sponsoring Agency Name and Address National Aeronautics and Space Administration Washington, D.C. 20546		14. Sponsoring Agency Code	
		15. Supplementary Notes	
16. Abstract A numerical method, which is simpler and more efficient than others currently in use, is proposed for the computation of the full viscous flow over an aerobrake body in hypersonic stream at high altitude. It treats the shock layer surrounding the blunt forebody and the near wake behind the base simultaneously by formulating the Navier-Stokes equations in conformal and azimuthal-angle coordinates. The computational domain is confined by the body wall, outflow surface and the bow shock, which is adjusted along the coordinate normal to the wall in the course of iterations. Because of the optimal grid and a well-developed alternating direction implicit factorization technique for the governing equations, reasonably accurate results can be obtained with a 28 x 36 x 7 grid and 400 time-marching iterations. Excellent agreement of shock location is found between the present result and the schlieren photograph. Details of the base flow and shear-layer impingement on the cylindrical aft body are presented for an adiabatic-wall case.			
17. Key Words (Suggested by Author(s)) Aerobrake Hypersonic flow and wake Computation method		18. Distribution Statement Unclassified - Unlimited Subject Category 02	
19. Security Classif. (of this report) Unclassified	20. Security Classif. (of this page) Unclassified	21. No. of Pages 17	22. Price*

*For sale by the National Technical Information Service, Springfield, Virginia 22161

